University of Kent

Kent Academic Repository

Greaves, Faye, Nassif, Vivian, Alfredsson, Maria, Chadwick, Alan V., Parmenter, Ryan, Cizek, Jacub, Melikhova, Oksana, Lei, Lei, Grant, David M., Dornheim, Martin and others (2026) ***The role of Al addition on the hydrogen sorption properties of TiVZrNbHf high entropy alloy.*** **Intermetallics, 189 . ISSN 0966-9795.**

Downloaded from

https://kar.kent.ac.uk/115278/ The University of Kent's Academic Repository KAR

The version of record is available from

https://doi.org/10.1016/j.intermet.2025.109119

This document version

Publisher pdf

DOI for this version

Licence for this version

CC BY (Attribution)

Additional information

Versions of research works

Versions of Record

If this version is the version of record, it is the same as the published version available on the publisher's web site. Cite as the published version.

Author Accepted Manuscripts

If this document is identified as the Author Accepted Manuscript it is the version after peer review but before type setting, copy editing or publisher branding. Cite as Surname, Initial. (Year) 'Title of article'. To be published in ***Title of Journal*** , Volume and issue numbers [peer-reviewed accepted version]. Available at: DOI or URL (Accessed: date).

Enquiries

If you have questions about this document contact ResearchSupport@kent.ac.uk. Please include the URL of the record in KAR. If you believe that your, or a third party's rights have been compromised through this document please see our Take Down policy (available from https://www.kent.ac.uk/guides/kar-the-kent-academic-repository#policies).

Intermetallics 189 (2026) 109119

Contents lists available at ScienceDirect

Intermetallics

journal homepage: www.elsevier.com/locate/intermet

The role of Al addition on the hydrogen sorption properties of TiVZrNbHf high entropy alloy

Faye Greaves [a], Vivian Nassif [b], Maria Alfredsson [c], Alan V. Chadwick [c], Ryan Parmenter [c], Jakub Čížek [d], Oksana Melikhova [d], Lei Lei [e], David M. Grant [e], Martin Dornheim [e], Sanliang Ling [e], Patrick Cullen [f], Claudia Zlotea [a,*]

[a] Univ. Paris Est Creteil, CNRS, ICMPE, UMR 7182, 2 Rue Henri Dunant, 94320 Thiais, France
[b] University Grenoble Alpes, CNRS, Institut Néel, 38000 Grenoble, France
[c] Materials Energy and ElectronicsGroup, School of Chemistry and Forensic Sciences, University of Kent, Kent, Canterbury, CT2 7NH, UK
[d] Faculty of Mathematics and Physics, Charles University, V Holesovickach 2, Prague 8 18000, Czech Republic
[e] Advanced Materials Research Group, Faculty of Engineering, University of Nottingham, Nottingham NG7 2RD, UK
[f] School of Engineering and Materials Science, Queen Mary University of London, Mile End Road, London E1 4NS, UK

ARTICLE INFO

Keywords:
High entropy alloys
Hydrides
Hydrogen storage
Phase transition
Dislocations
Vacancy

ABSTRACT

Refractory BCC high entropy alloy TiVZrNbHf is a promising material for solid-state hydrogen storage with high hydrogen sorption capacity but unfavourable thermodynamics of hydride phase, *i.e.* too stable hydride that need high temperature to reversibly recover the absorbed hydrogen. As an attempt to destabilize the hydride phase, this study reports on the effect of Al addition (limited concentrations: 5 and 10 at.%) into this alloy on the physicochemical and hydrogen sorption properties. Despite traces of a V-Al secondary phase, the BCC $(TiVZrNbHf)_{1-x}Al_x$ alloys are random solid solutions which form high-capacity FCC hydride phases under hydrogen atmosphere at room temperature, as proven by synchrotron and neutron diffraction. Although Al decreases the hydrogen sorption capacity, the presence of a *p* element destabilizes the FCC hydride phase. A comparison with previous literature data helps understanding the role of Al which strongly depends on the chemical composition of the initial alloys. XANES studies allowed access to details of the electronic structure of the unoccupied levels complemented by density functional theory calculations. Moreover, the addition of Al favours the formation of larger open volume defects during hydride formation than the initial Al-free alloy which might explain the faster absorption kinetics in Al-containing alloys.

1. Introduction

Year on year new technology is under development to move away from fossil fuels towards more sustainable and cleaner energy solutions. Hydrogen within the realm of renewable energy is notable as a clean and efficient carrier of energy. Yet utilising hydrogen for application faces several challenges which are defined by low-emission production and comprehensive storage[1–3]. While physical storage of hydrogen is presently a more mature method, metal hydrides, i.e. compounds between metals and hydrogen atoms with high hydrogen/metal (H/M) ratio, are an appealing alternative for safe, stable and efficient solid-state storage, including providing reversible absorption and desorption under controlled temperature and pressure conditions [4,5]. In this context, a contemporary type of materials has gained attention, namely high-entropy alloys (HEAs). These materials are characterized by having five or more metallic elements in equimolar or proximate concentrations, ranging from 5 to 35 at.%. Initially introduced by Yeh et al. and Cantor et al., HEAs exhibit a wide range of compositions and thermal stability, making them promising candidates for various applications, including hydrogen storage materials [6,7]. The multi-component nature of HEAs introduces complex interactions that can influence their structural stability, hydrogen absorption kinetics, and overall performance. The high mixing entropy is not the only factor that influences the solid solution formation in multi-component alloys. The formation of a solid solution requires that the mixing enthalpy (ΔH_{mix}), atomic size difference (δ) and mixing entropy (ΔS_{mix}) simultaneously satisfy certain ranges [8]. For single-phased solid solutions the requirements are more restrictive, in which a more negative ΔH_{mix} is

* Corresponding author.
E-mail address: claudia.zlotea@cnrs.fr (C. Zlotea).

https://doi.org/10.1016/j.intermet.2025.109119
Received 18 August 2025; Received in revised form 24 November 2025; Accepted 1 December 2025
Available online 5 December 2025
0966-9795/© 2025 The Authors. Published by Elsevier Ltd. This is an open access article under the CC BY license (http://creativecommons.org/licenses/by/4.0/).

preferred, and a lower atomic size difference, $\delta < 6.6$ [9]. Further, the valence electron concentration (VEC) plays a role into the stability and prediction of the phase formed where: VEC <6.87 a body-centred cubic (BCC) structure is favoured, VEC >8 a face-centred cubic (FCC) phase is preferred, a mixture of the two phases can be likely found between 6.87 and 8 [10].

Aluminium (Al) has been suggested as an alloying element in high-entropy alloys due to its favourable light weight and high specific strength ratio and this has led to studies into creating Al containing HEAs [11]. The use of Al as an alloying element may increase the gravimetric storage capacity of hydrogen however, to date the number of studies is limited.

A number of HEAs have been explored to produce a BCC structure. The MgAlTiFeNi studied by Cardoso et al. was synthesised through ball-milling (BM) under inert atmosphere and reactive ball-milling (RBM) under a hydrogen atmosphere [12]. The alloy formed was a single-phased BCC structure after BM, though showed a mixture of BCC and FCC hydride phases after RBM, alongside a capacity of 0.94 wt%. Similarly, the alloy of MgAlVCrNi was produced through RBM also demonstrating a BCC hydride phase but with relatively low capacity (0.3 wt%) [13]. While seemingly discouraging capacities of hydrogen, these studies indicate that best solutions for hydrogen storage are alloys with an increase in the proportion of hydride-forming elements.

At the same time, Montero et al. investigated a 10 % addition of Al to the quaternary alloy of $Ti_{0.325}V_{0.275}Zr_{0.125}Nb_{0.275}$ which contains only hydride-forming elements [14]. The Al-containing alloy was synthesised through electric arc-melting, producing a BCC structure and studied its hydrogen sorption properties. The findings showed a maximum capacity of 1.6 H/M, lower than the equimolar TiVZrNb (2.0 H/M) [15] or the non-equimolar $Ti_{0.325}V_{0.275}Zr_{0.125}Nb_{0.275}$ (1.8 H/M) [16,17]. However, the alloy showed fast kinetics in terms of hydrogen absorption at 25 °C, giving a body-centred tetrahedral (BCT) hydride phase. Overall, the findings suggested that the addition of 10 % Al destabilizes the $Ti_{0.325}V_{0.275}Zr_{0.125}Nb_{0.275}$ alloy, decreasing the temperature of desorption, and improving its cycling abilities.

Later, Pineda-Romero et al. also studied the effects of the addition of Al to the ternary alloy of TiVNb, where $Al_x(TiVNb)_{1-x}$ and $x = 0.05$, 0.1, 0.175, and 0.25 [18,19]. Initially, adding 10 at.% Al ($x = 0.1$) showed a less stable hydride than the ternary one but at the expense of the capacity. The capacity is strongly affected by Al addition and decreases below 1 H/M for compositions containing more than 15 at% Al. For the alloy with lower content of Al ($x = 0.05$) the capacity was improved (1.84 H/M) but the effects of increased destabilization were more limited. In summary, the addition of Al in TiVNb and TiVNbZr-based alloys destabilizes the thermodynamics of corresponding hydride phases, *i.e.*, the hydrogen desorption occurs at lower temperature, but on the expense of the storage capacity. From these previous studies, it is suggested that a maximum of 10 at.% Al addition is a viable trade-off between thermodynamic destabilization and limiting loss of capacity.

The quinary TiVZrNbHf composition has been comprehensively studied for its high-capacity and formation of single-phased stable alloy and hydride [16,20,21]. Despite a promising capacity, it forms a very stable dihydride [20], desorbing at temperatures over 300 °C. Therefore, as an extension of previous studies, a possible way to destabilize this promising quinary composition and desorb hydrogen at lower temperature is to add small amount of Al.

In this perspective, the scope of this manuscript is to study the effect of Al addition at 5 and 10 at.% to the TiVZrNbHf alloy on the physico-chemical and hydrogen sorption properties. A series of three alloys were prepared $(TiVZrNbHf)_{1-x}Al_x$ where $x = 0$, 0.05, 0.10 and characterized by laboratory and large-scale facilities. This includes in-depth analysis of local and electronic structures of these new alloys and corresponding hydrides by synchrotron radiation. The phase transition during desorption from the highest Al-content hydride phase was followed by *in situ* neutron diffraction. Finally, a systematic study of crystalline defects formed after one absorption cycle was carried out by positron annihilation spectroscopy to clarify the role of Al on hydrogen sorption properties.

2. Experimental

2.1. Synthesis of alloys

The synthesis of a TiVZrNbHf alloy was previously reported [22] and around 3 g of $(TiVZrNbHf)_{0.95}Al_{0.05}$, and $(TiVZrNbHf)_{0.90}Al_{0.1_0}$ were synthesised using electric arc-melting (90 A) under an argon atmosphere (0.3 bar). Firstly, pre-alloys of higher melting temperature elements (Ti, V, Zr, Nb, and Hf) were prepared. Al was then added and hidden beneath the pre-alloy ingot with a lower current (70 A). The final ingot was melted a further 10 times to homogenise, flipping between each melt. Bulk material of Ti, V, Zr, Nb, and Hf pellets (NEYCO Vacuum-&Materials, 99.9+ %), and Al (99 % pure, STREM Chem) were utilized. The resulting buttons were cut using a high-precision saw (Buehler Isomet 1000) to obtain flat surfaces for structural characterization.

2.2. Structural & microstructural characterization

Structural characterization of the as-cast bulk and powdered material (hydrogenated and desorbed material) was carried out by X-ray diffraction (XRD) using a D8 Advance Bruker diffractometer (Cu K_α radiation $\lambda = 1.5406$ Å, Bragg-Brentano geometry). Microstructural analysis was conducted *via* scanning electron microscopy (SEM) using a Zeiss Merlin instrument with an energy-dispersive X-ray spectroscopy (EDS) detector from Oxford Instruments. As-cast sample was embedded in epoxy resin, polished, and coated with a 0.8–1.0 nm Pd layer. Elemental quantification used an accelerated electron voltage of 20 keV, detecting K_α lines for Ti, V, and Al, and L_α lines for Nb, Zr, and Hf.

2.3. Hydrogen absorption measurements

Hydrogenation was performed on ~0.3 g of as-cast pieces of alloy through utilization of the Sieverts' method which consists of a home-made manometric device with thermostatically calibrated volumes. The stainless-steel sample holder was filled with the sample, fitted with metal gaskets to prevent gas leaking, and then sealed before connecting to Sieverts' apparatus. The activation process for each of the materials was carried out by heating the sample to 350 °C for 3 h under dynamic vacuum (2.0×10^{-3} mbar), followed by cooling to the working temperature. The initial hydrogen absorption kinetics was conducted by applying approximately 50 bar H_2 at 25 °C while recording the pressure variation. The capacity and weight percentage of each alloy were determined using the real gas state equation for H_2 (GASPACK version 3.32, Horizon Technologies). Desorption was achieved by heating the samples at a rate of 5 °C/min from 25 to 450 °C under dynamic secondary vacuum. After one full cycle of hydrogen absorption and desorption, the alloys became brittle and could be ground into powder for further studies.

2.4. Neutron and synchrotron X-ray diffraction

In situ and *ex situ* neutron diffraction experiments were performed at the D1B beamline ($\lambda = 1.28$ Å) at the Institut Laue-Langevin (ILL) in Grenoble, France (http://doi.ill.fr/10.5291/ILL-DATA.5-22-832). Initially, fully deuterated samples (~3 g) were prepared in a similar fashion as described above under approximately 50 bar of D_2 pressure at 25 °C with same activation procedure. *Ex situ* measurements were performed in V sample-holders at 25 °C, over a scanning range of 1–128° (2θ) with a 50-min scan duration. Subsequently, for *in situ* measurement, $(TiVZrNbHf)_{0.9_0}Al_{0.10}$ fully deuterated powder was placed into a silica capillary and heated under dynamic vacuum (~1×10^{-5} mbar) from 25 to 450 °C at a constant rate of 1 °C/min, as previously reported for pristine deuterated TiVZrNbHf [22]. A thermocouple was connected to

the top of the sample-holder and placed in contact with the powder sample inside the silica tube, while the released deuterium pressure was monitored using a vacuum gauge. Structural characterization of the *ex-situ* diffraction patterns was conducted using Rietveld analysis in FullProf software, with peak shapes described by the Thompson-Cox-Hastings Pseudo-Voigt function. The lattice parameters during thermal evolution were determined using Le Bail fitting in FullProf [23].

Ex-situ synchrotron X-ray diffraction (SR-XRD) was performed at the ID15A beamline at the European Synchrotron Radiation Facility (ESRF) in Grenoble, France [24]. Hydrogenated and desorbed powdered samples were prepared in borosilicate capillaries for total scattering experiments and subsequent the pair distribution function (PDF) analysis. The incident beam energy was 98 keV ($\lambda = 0.1265$ Å), and diffraction patterns were recorded using a Pilatus 2M CdTe detector, then azimuthally integrated *via* the pyFAI library [25]. Each sample was measured by slightly adjusting the detector's position to ensure homogeneity of the powdered sample. G(r) profiles were obtained from the integrated patterns using pdfgetx3 [26] while the local structural analysis was carried out using the small-box approach implemented in the PDFgui [27] free software. The average structure was determined from SR-XRD patterns by using the Rietveld analysis implemented in FullProf software [23].

2.5. Positron annihilation spectroscopy

Positron annihilation spectroscopy (PAS) was employed for characterization of lattice defects in as-cast $(TiVZrNbHf)_{1-x}Al_x$ alloys and their hydrides. A ^{22}Na radioisotope with activity of ≈1 MBq deposited on 7.5 μm thick Kapton foil was used as a positron source. Positron lifetime measurements [28] were carried out using a digital spectrometer [29] with the time resolution of 144 ps (FWHM of resolution function for ^{22}Na). At least 10^7 positron annihilation events were collected in each spectrum. Decomposition of positron lifetime spectra into individual components was performed using a PLRF code [30]. The source contribution to positron lifetime spectra was determined using the procedure described in Ref. [31].

Coincidence Doppler broadening (CDB) spectroscopy [32] was employed for characterization of local chemical environment of defects. CDB investigations were conducted using a digital spectrometer [33] equipped with two HPGe detectors. The energy resolution of the CDB spectrometer is 0.9 keV at 511 keV and peak-to background ratio is higher than 10^5. At least 10^8 annihilation events were collected in each CDB spectra. The results of CDB investigations are presented in the paper as ratio curves related to well annealed pure Al (99.9999 %) reference.

2.6. X-ray absorption spectroscopy

X-ray Absorption Spectroscopy (XAS) measurements were made for all transition metals present in the alloys (Ti, V, Zr, Nb and Hf) on beam line B18 at the Diamond Light Source at the Harwell Campus, UK. The beam line is equipped to measure quick EXAFS in transmission and fluorescence mode and a third ion chamber is used to collect transmission spectra from a reference metal foil for energy calibration. The monochromator used in all measurements is the Si(111), while the Pt 3rd harmonic mirror was employed in the V and Ti K-edge and Hf L_3-edge experiments, the Cr optical branch was the used for the Zr and Nb K-edge measurements. Nb K-edge, Zr K-edge and Hf L_3-edge spectra were measured in transmission mode on pellets of powdered alloys and cellulose. V K-edge and Ti K-edge spectra were measured in fluorescence mode on powdered alloy samples. Where possible the energy range of the spectra covered both the near-edge region (XANES) and the extended fine structure region (EXAFS). The XANES data treatment (pre-edge subtraction and normalization) was performed by the help of the MAX program package [34,35].

2.7. Density functional theory calculations

TiVZrNbHf and $(TiVZrNbHf)_{0.90}Al_{0.10}$ alloy structures in the *bcc* phase were constructed using a $3 \times 3 \times 3$ supercell comprising 54 metal atoms. Corresponding dihydride structures with FCC symmetry were generated using a $3 \times 2 \times 2$ supercell containing 48 metal atoms. Density Functional Theory (DFT) calculations, including geometry optimisation and density of states (DoS) calculations, were performed using the Vienna Ab initio Simulation Package (VASP) [36]. For structural optimisation, a plane-wave basis set with a kinetic energy cutoff of 400 eV was employed to expand the wave functions. We used the Perdew-Burke-Ernzerhof (PBE) exchange-correlation functional [37] in conjunction with the projector augmented wave (PAW) method [38,39] to solve the Kohn-Sham equations. To enhance convergence of the electronic self-consistent field (SCF) calculations, a first-order Methfessel-Paxton smearing [40] with a width of 0.2 eV was applied. A k-point mesh with a spacing of approximately 0.20 $Å^{-1}$ was used, and the energy convergence criterion was set to 10^{-4} eV. These parameter choices were validated by convergence tests showing negligible structural variations compared to stricter settings, consistent with established literature benchmarks. [41–43]. Structural relaxation, including optimisation of cell parameters and atomic positions, was deemed converged when the maximum force on any atom was below 0.05 eV/Å. For DoS calculations, more stringent SCF calculations were conducted using the optimised geometry, with a kinetic energy cutoff of 520 eV and an energy convergence threshold of 10^{-6} eV. DoS calculations were performed by restarting from the resulting charge density, employing the same energy cutoff and convergence settings, with tetrahedron smearing and a total of 1200 bands. To enable better comparison, we normalized the projected DoS intensity with the total number of valence electrons for each element.

3. Results and discussion

3.1. Crystalline structure of alloys and hydrides

The series of $(TiVZrNbHf)_{1-x}Al_x$ alloys with $x = 0$, 0.5 and 0.10 prepared by arc melting are mainly BCC phases with a small secondary phase for Al-containing samples, as illustrated in the SR-XRD patterns (Fig. 1a). The BCC lattice parameters decrease with increasing Al content (Table 1) as also confirmed by DFT modelling. This is reasonably explained by the relatively small Al atomic size among all components: $r_V = 1.31$ Å $< r_{Al} = r_{Nb} = 1.43$ Å $< r_{Ti} = 1.45$ Å $< r_{Hf} = 1.56$ Å $< r_{Zr} = 1.59$ Å [44]. Empirical parameters derived from HEA composition such as, δ (mean square deviation of atomic size) and VEC (valence electron concentration), are listed in Table 1. The δ is close or slightly above the empirical limit 6.6 % proposed for substitutional solid solutions in HEAs [45]. This might explain the presence of a small secondary phase for $x = 0.05$ and 0.10. The VEC values are inferior to 5, which confirms that BCC phases are expected [10].

These alloys absorb hydrogen under 50 bar H_2 pressure at 25 °C, as illustrated in the absorption kinetic curves in Fig. 1b. The Al presence strongly enhances the initial step of absorption kinetics on the expenses of maximum capacity which drops from 2.0 to 1.75 and 1.70 H/M with increasing Al content (Fig. 1b and Table 1). This decreasing trend was already observed in other Al-containing HEAs [46] and one possible explanation is that Al is the only non-hydride forming element among all metallic components in this series of alloys. The formed dihydrides adopt an FCC lattice, as shown by SR-XRD on hydrogenated phases (Fig. 1c) and neutron diffraction on deuterated samples (Fig. 1d). Small traces of a secondary phase are also present in the SR-XRD diagrams (Fig. 1c) that are usually interpreted as incomplete hydrogenated BCC phases. The FCC lattice parameters, as determined from structural refinements of SR-XRD data, decrease with increasing Al content, in line with the trend found in the initial BCC alloys (Table 1) and DFT calculations. The refinements of neutron diffraction data suggest that D atoms

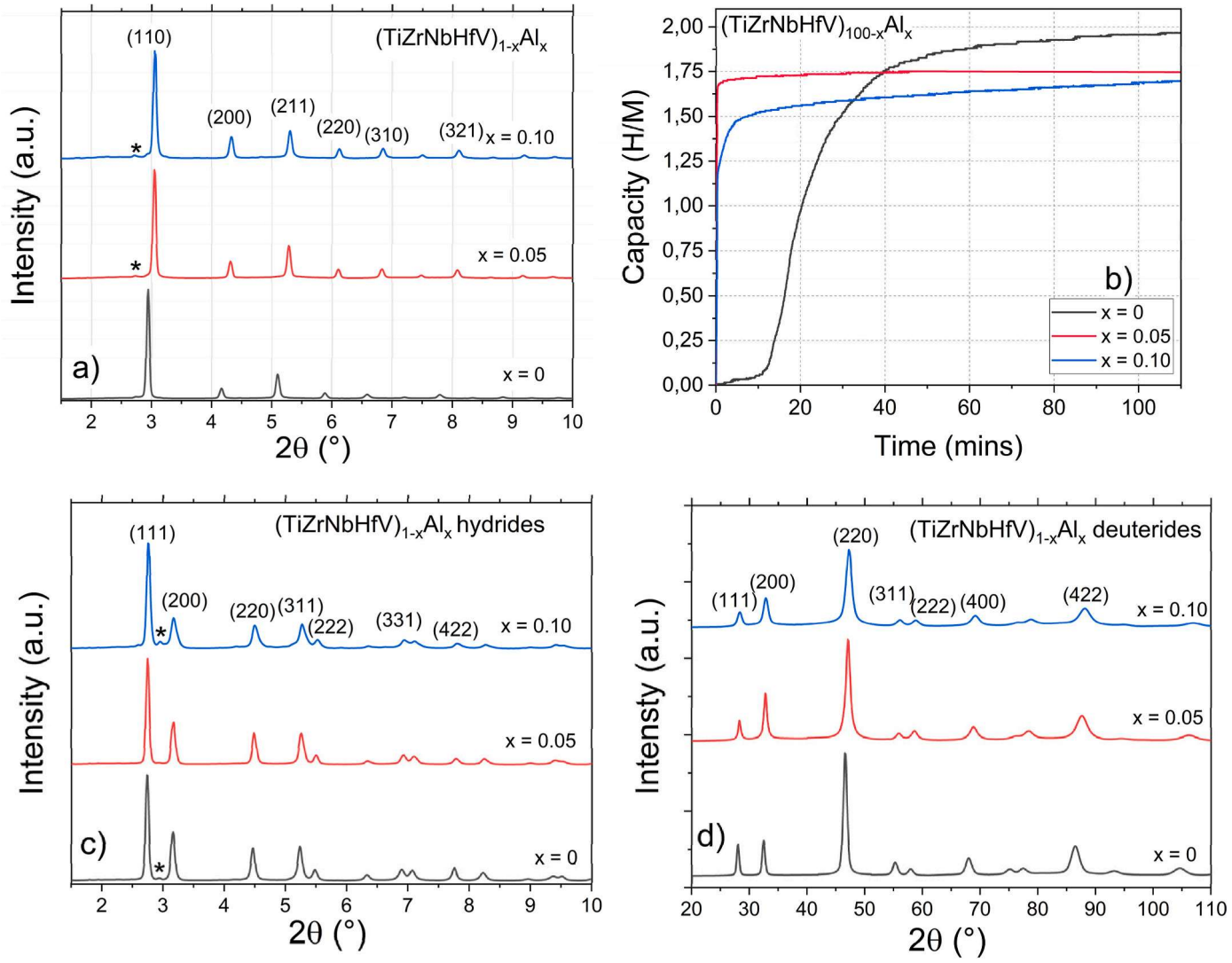


Fig. 1. a) SR-XRD ($\lambda = 0.1265$ Å) patterns of $(TiVZrNbHf)_{1-x}Al_x$ alloys with $x = 0$, 0.05 and 0.10; b) Absorption kinetic curves at 25 °C under around 50 bar H_2 pressure; c) SR-XRD ($\lambda = 0.1265$ Å) patterns of corresponding hydride phases; d) neutron diffraction ($\lambda = 1.28$ Å) patterns of deuteride phases. The minor secondary phases initially present in the alloys are marked with an asterisk in panels a) and c).

Table 1
Physicochemical parameters of the $(TiVZrNbHf)_{1-x}Al_x$ alloys with $x = 0$, 0.05 and 0.10: lattice distortion (δ), VEC, lattice parameters of the initial BCC alloys (from XRD and DFT modelling), FCC hydrides (from SR-XRD), FCC deuterides (from neutron diffraction) and DFT modelling and hydrogen absorption capacity (H/M).

$(TiVZrNbHf)_{1-x}Al_x$	Al content, x	δ (%)	VEC	Lattice Alloy	a_{BCC} (Å)		Lattice Hydride/ deuteride	a_{FCC} (Å)			Capacity (H/M)
					XRD	DFT		Hydride *SR-XRD*	Deuteride *neutron diffraction*	DFT	
TiVZrNbHf	0	6.82	4.4	BCC	3.381 (4)	3.345	FCC	4.588 (2)	4.547 (3)	4.548	2.0
$(TiVZrNbHf)_{0.95}Al_{0.05}$	0.05	6.68	4.3	BCC	3.351 (2)	–	FCC	4.565 (2)	4.521 (3)	–	1.75
$(TiVZrNbHf)_{0.90}Al_{0.10}$	0.10	6.53	4.2	BCC	3.339 (2)	3.331	FCC	4.558 (3)	4.512 (3)	4.537	1.70

are located into the tetrahedral sites (¼ ¼ ¼) of the FCC lattice, in good agreement with previous results on HEAs [47]. Moreover, the refined occupancy of D follows the same reducing trend as the capacity values measured during hydrogenation with Al content: 2.0, 1.8 and 1.7 D/M for $x = 0$, 0.05 and 0.10, respectively.

Rietveld refinement results for alloys/hydrides/deuterides are given in section 1 of supplementary material whereas section 2 details the microstructural analyses by SEM-EDS. The observed dendritic microstructure of these alloys is typical for refractory HEAs [22], while the presence of a minor secondary V-Al phase is confirmed in both Al-containing alloys, in line with SR-XRD data (Fig. 1a). The average chemical composition by SEM-EDS confirms the nominal value, irrespective of alloy, as shown in the supplementary material.

3.2. *Local structure from PDF analysis*

Previous results on Al-containing HEA have suggested a short-range order and pairing of Al with Ni and Cu atoms [48]. Thus, it is important to study the local structure in Al-containing HEAs and understand the Al effect on the atom-scale distribution. From total X-ray scattering we could extract the pair distribution function (PDF) profile for both BCC alloys and FCC hydrides (Fig. 2) and the small-box refinements results

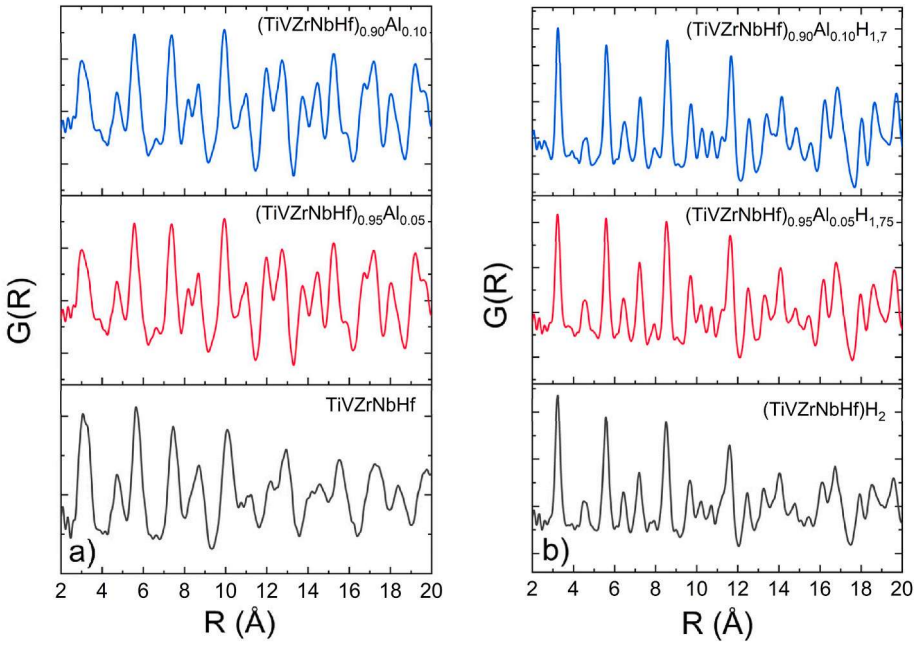


Fig. 2. PDF profiles from SR-X-ray total scattering for $(TiVZrNbHf)_{1-x}Al_x$ alloys (left) and corresponding hydrides (right) with $x = 0$, 0.05 and 0.10.

are listed in Table 2.

These SR-XRD measurements were performed on powder samples: the dihydrides are already in powder form after first hydrogen absorption while the BCC phases were prepared by one absorption/desorption cycle as the as-cast alloys are difficult to break into powder by usual mechanical means. The lattice parameters of FCC dihydride phases obtained from PDF analysis are in good agreement with XRD results (Table 1). However, the BCC lattice parameters are slightly larger than the as-cast alloys. This can be understood as these powders are desorbed materials after one absorption/desorption cycle and might contain a small amount of trapped H which slightly increases the BCC lattice parameters. The isotropic atomic displacement factors (U_{iso}) are larger in the BCC desorbed phases than in the FCC dihydrides. This might hint to an effect of trapped H atoms on the static atomic disorder in the desorbed materials relative to the hydrides with a well-ordered distribution of H atoms in the tetrahedral sites, as proven by neutron diffraction. Overall, the PDF analysis confirms a decreasing trend in lattice parameters with increasing Al content for both BCC and FCC phases.

The PDF analysis uses a small-box approach, which describes the unit cell as a random atomic distribution on the same crystallographic site, irrespective of lattice. The differences between the experimental points and the PDF fit are negligible (see section 3 in the supplementary material). This points out that despite the presence of many elements into these alloys, the atoms seem to be randomly distributed without segregation or preferential pairing of atoms suggesting the formation of solid solutions in both alloy and hydride forms.

3.3. XANES study

To complement our structural findings, a XANES study has been performed as this technique can provide useful information on the electronic structure of the unoccupied energy levels. Only two compositions $(TiVZrNbHf)_{1-x}Al_x$ with $x = 0$ and 0.10 have been completely measured at the K-edges of Ti (4.966 keV), V (5.465 keV), Zr (17.997 keV) and Nb (18.985 keV) and the L_3-edge of Hf (9.56 keV) as both alloy and dihydride phases (see Fig. 3).

The XAS K-edge of *d* transition metals results from electric dipole transitions from 1*s* to continuum state according to the selection rules, while the pre-peak corresponds to transition from 1*s* to hybridized *p-d* states and is usually of small amplitude [49]. The position of the K-edge electric dipole-allowed $1s \rightarrow 4p$ transitions can inform on the oxidation state of the absorbing atom: the higher the effective charge of an atom, the more energy is required to ionize a core electron which may shift the absorption edge to higher energies. The pre-peaks are electric quadrupole-allowed transitions $1s \rightarrow$ mixed *p-d* and their position and intensity are sensitive to the oxidation state, coordination, and symmetry of the coordination sphere. In hydrides, the pre-peak might be due to a transition of a 1*s* electron into a mixed *d*-H *s* state [50].

The normalized XAS spectra at the Ti and V K-edges show recognizable absorption edges but the EXAFS regions are ill-defined (Fig. 3a and b). Both alloys show small pre-peaks at close positions to Ti and V references, respectively, while this peak almost vanishes in the corresponding hydrides. The vanishing of the pre-peak in the dihydride phases is mainly due to the filling of the mixed *p-d* band with *s* electrons from H atoms, as confirmed by DFT modelling in the next section. Empty states in the hybridized *p-d* are less available in hydrides and thus number of transitions from 1*s* core level are reduced.

XAS spectra at Zr and Nb K-edges, are better resolved after the absorption edge, however the EXAFS oscillations are rather weak as compared to pure metal references making the analysis of local structure unfeasible. A small feature in the pre-edge is also noticeable for these edges for both alloys while it completely vanishes for hydrides. Similar

Table 2
PDF analysis of SR-X-ray total scattering data for the $(TiVZrNbHf)_{1-x}Al_x$ alloys and corresponding hydrides with $x = 0$, 0.05 and 0.10: lattice type, lattice parameters and isotropic atomic displacement factor (U_{iso}).

$(TiZrNbHfV)_{1-x}Al_x$	Al content, *x*	Lattice alloy	a_{BCC} (Å)	U_{iso} (Å^2)	Lattice hydride	Capacity (H/M)	a_{FCC} (Å)	U_{iso} (Å^2)
TiVZrNbHf	0	BCC	3.412 (7)	0.031 (15)	FCC	2.0	4.586 (2)	0.012 (2)
$(TiVZrNbHf)_{0.95}Al_{0.05}$	0.05	BCC	3.358 (2)	0.025 (5)	FCC	1.75	4.568 (2)	0.011 (2)
$(TiVZrNbHf)_{0.90}Al_{0.10}$	0.10	BCC	3.346 (2)	0.019 (3)	FCC	1.70	4.550 (5)	0.012 (4)

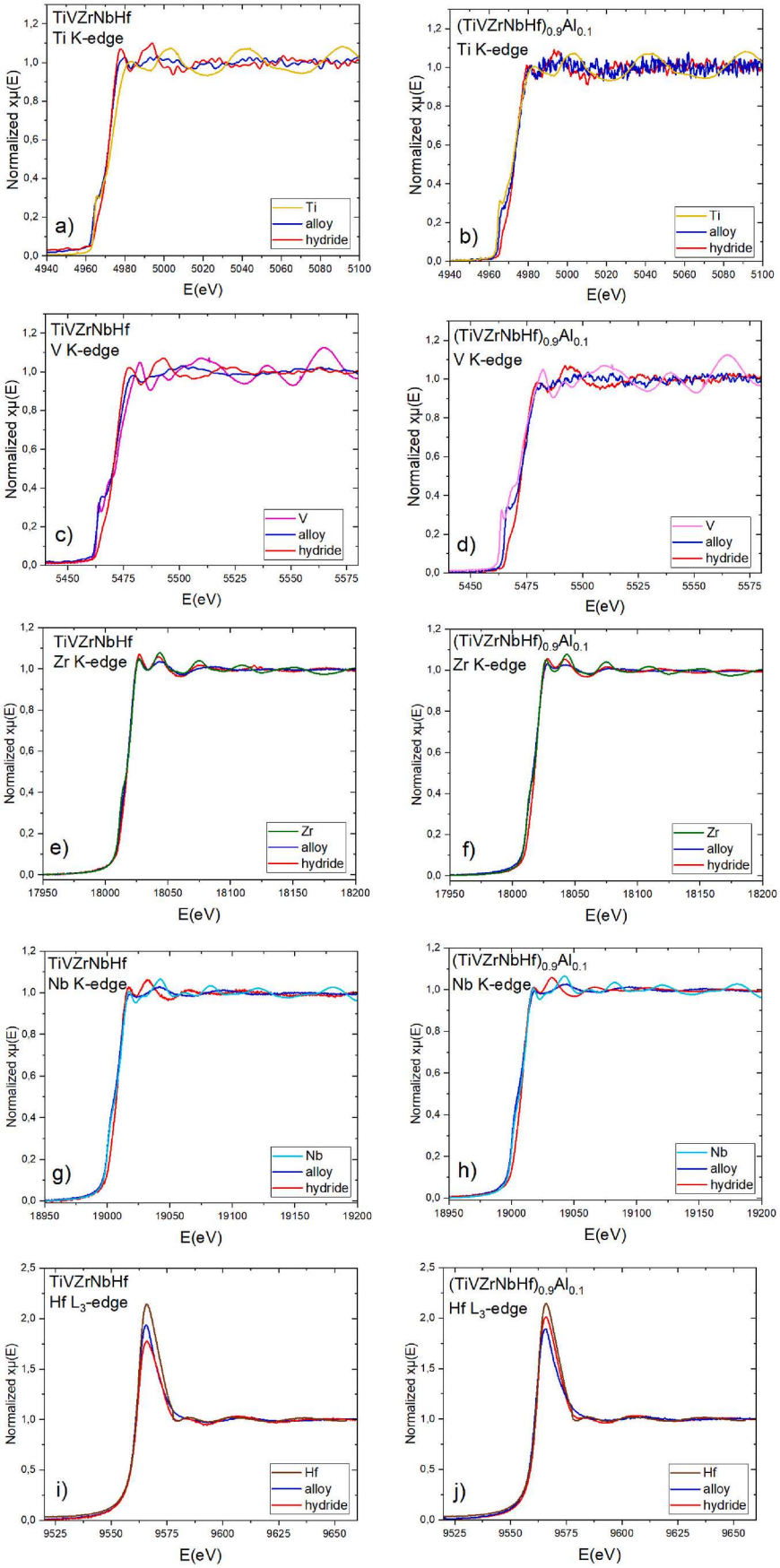


Fig. 3. XANES spectra at Ti, V, Zr and Nb K-edges and Hf L_3-edge for $(TiVZrNbHf)_{1-x}Al_x$ alloys and corresponding hydrides with $x = 0$ (left column) and 0.10 (right column). The absorption edges of the corresponding pure metals are also shown for each element.

explanation as above can be put forward.

The XAS L_3-edge corresponds to 2*p* electron transitions to continuum state with a strong characteristic white line (WL) which reflects the high density of states just above the Fermi level. The Hf L_3-edge are due to the excitation of $2p_{3/2}$ into the Hf 5*d* states showing a large WL for both alloys and dihydrides though their amplitude is reduced as compared to pure Hf reference. This points out to a filling of the *d* band by alloying with V and Nb which possess larger number of *d* electrons then Ti, Zr and Hf, as also reflected by an increased VEC (4.2–4.4) as compared to VEC for pure Hf (4). However, the amplitude of the WL varies after hydride formation: for the Al-free alloy, the WL decreases in the dihydride while for Al-containing alloy it increases. Previous results have shown that the electrochemical formation of hydride in $LaNi_5$ compound causes a depletion in the La 5*d* orbital vacancy which is mirrored by an increase in the magnitude of the WL [51].

For further analysis, the intensity of the Hf L_3-edge WL was calculated as the area after extraction of an arctangent background from the XANES spectra, see section 4 of supplementary information. The intensity varies inversely with the Al concentration. The initial alloy TiVZrNbHf ($x = 0$) presents a lower intensity of the WL as hydride relative to the alloy, while the WL intensity of both Al-containing alloys ($x = 0.05$ and 0.10) is higher for dihydrides than alloys (see section 4 of supplementary information).

3.4. Electronic DOS from DFT modelling

Further insights into the electronic density of states (DOS) of both alloy and hydride phases are given by DFT theoretical calculation. The orbital (*spd*) projected density of states (pDOS) for all involved metals and H atoms in TiVZrNbHf and $(TiVZrNbHf)_{0.90}Al_{0.10}$ as initial BCC alloys and FCC hydride phases are shown in Fig. 4. The pDOS features of both alloys are very similar showing a metallic character. The *d* orbitals of Ti, V, Zr, Nb and Hf are dominating in the energy range of −4 to 10 eV with a strong hybridization between these elements that might be responsible for the stability of the alloys, irrespective of composition. In the $(TiVZrNbHf)_{0.90}Al_{0.10}$ alloy, Al contributes to pDOS with both *s* and *p* states while the *s* orbital is found at lower energies than the *p* orbitals. The pDOS profiles for both hydride phases are comparable for metals and H atoms, regardless of the composition. The Fermi levels lay in the metal *d* band which confirms the metallic character of hydride phases. The H *s* orbitals hybridize with the *s-p* and *d* states of all metals forming a low energy band below the Fermi level which suggest strong binding

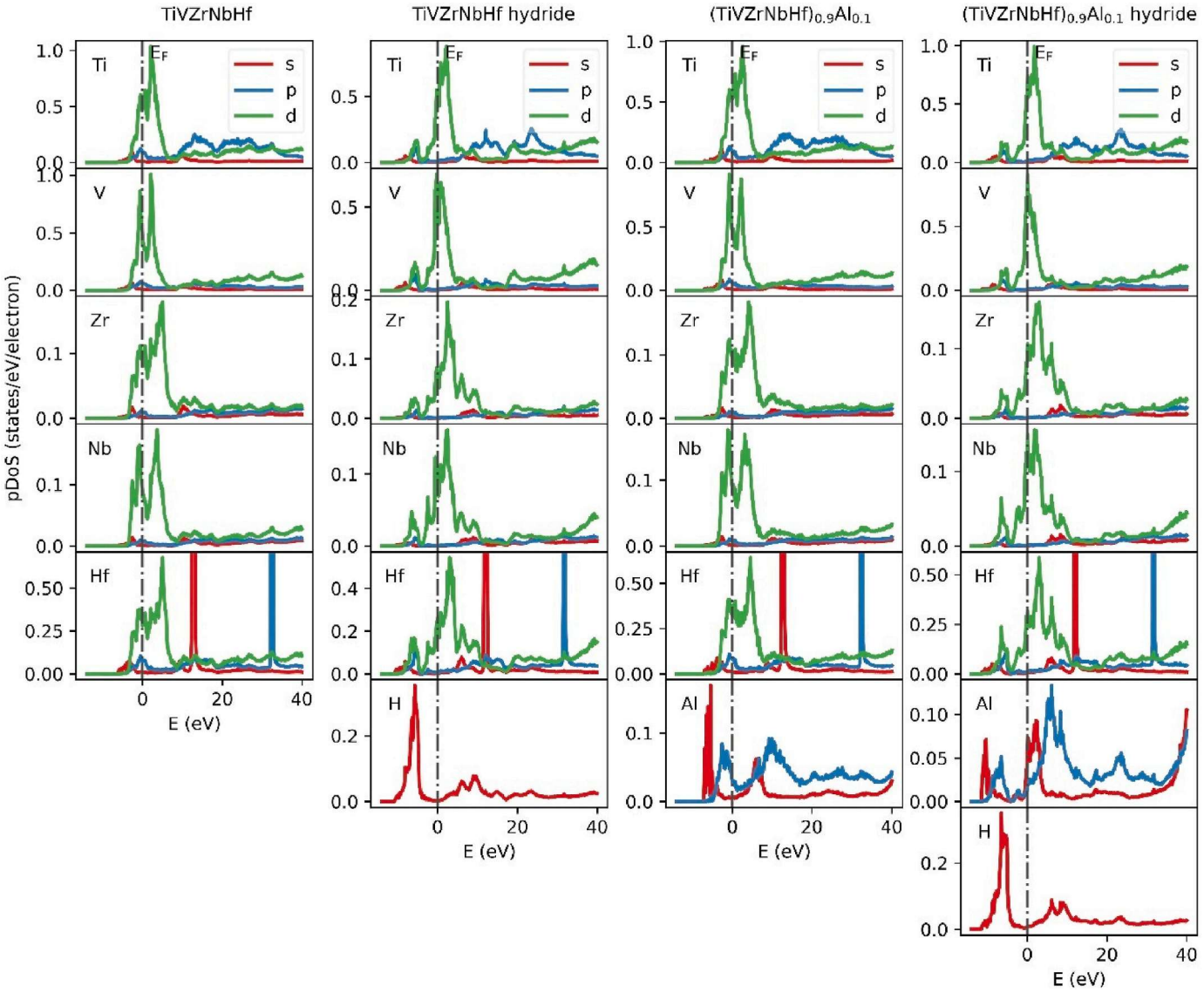


Fig. 4. Projected density of states for TiVZrNbHf and $(TiVZrNbHf)_{0.90}Al_{0.10}$ as initial BCC alloys and FCC hydride phases. The *s*, *p* and *d* states are plotted as red, blue, and green lines, respectively. The dotted line represents the Fermi level.

between the H and the metal elements. This hybridization with H *s* states delocalizes the metal states to lower energy as compared to alloy's pDOS, including Al *s-p* contribution. These results are in agreement with recent DFT calculation in similar HEA systems containing Al [52].

In summary, DFT calculations confirm that the H *s* orbitals hybridize with the *s-p* and *d* states of all metals forming a low energy bonding band below the Fermi level, which may explain the vanishing of the pre-peak in the XANES spectra of hydride phases at Ti, V, Zr and Nd at K-edges.

3.5. Phase transition during desorption by in situ neutron diffraction

Previously, we reported that the (TiVZrNbHf)H_2 undergoes a two-phase transition during deuterium desorption from an FCC dihydride (2 H/M) to a body-centred-tetragonal (BCT) monohydride (~1 H/M) and finally to a fully desorbed BCC phase [22]. A similar study was conducted here for the fully deuterated $(TiVZrNbHf)_{0.90}Al_{0.10}$ composition during deuterium desorption under vacuum by heating with a constant ramp (1 °C/min) starting from 27 to 450 °C.

Fig. 5 shows the neutron diffraction patterns recorded as a function of temperature on the left-hand side. The desorption gas profile recorded during the experiment is given in the middle panel while the thermal evolution of the lattice parameters for FCC and BCC phases, as determined by Le Bail refinement, is depicted on the right-hand side of Fig. 5.

As expected, a two-step phase transition was observed, in agreement with the earlier study [22]. The initial FCC phase begins desorbing deuterium around 150 °C with the maximum desorption rate at 190 °C which marks a sharp drop in the FCC's peaks intensity. Above 240 °C the FCC phase completely disappears and transforms to an intermediate BCT monodeuteride with low intensity diffraction peaks. This phase subsequently desorbs deuterium with a second maximum peak at 273 °C and reverts to the initial BCC lattice. The diffraction peaks of the intermediate and final desorbed phases are less intense as the FCC phase. This might be explained by a high disorder of D atoms in the BCT phase and a low scattering length of the metal network in the BCC desorbed material. Thus, Le Bail fitting could only be performed for the BCC phase, and a clear decrease of BCC lattice parameter is noticed due to deuterium desorption. This desorption transition sequence is also supported by the gas-desorption profile where the desorption peaks correspond to specific thermal events: the first small one relates to the beginning of the FCC to BCT phase transition, the main one determines the BCT to BCC phase transition while the last broad feature can be linked to the desorption from the BCC solid solution with hydrogen. This experiment confirms the full reversibility of absorption/desorption reactions in the Al-containing alloy.

Fig. S9 in the supplementary information (Section 5) compares the thermal stability of different hydride phases (FCC and BCT) for both TiVZrNbHf and $(TiVZrNbHf)_{0.90}Al_{0.10}$ hydrides, as determined by *in situ* neutron diffraction under similar conditions [22]. While the former alloy also begins to desorb deuterium at the same temperature (150 °C) the presence of 10 at. % Al decreases the temperature of the FCC → BCT phase transition from 278 °C to 190 °C. Hence, a destabilization of the FCC hydride phase can be suggested. A shift of the BCT → BCC transformation can be seen to a lesser extent from 300 °C to 273 °C. A working hypothesis based on the variation of Pauling electronegativity can be suggested to explain this finding, as already proposed for related HEAs compositions [43]. The average values of Pauling electronegativity for the two alloys are 1.48 and 1.49 for TiVZrNbHf and $(TiVZrNbHf)_{0.90}Al_{0.10}$, respectively. Al slightly increases the average electronegativity which decreases the mismatch with H electronegativity value (2.2). Consequently, this might weaken the metal–H interaction and lowers the hydride phase stability. Another possible explanation is based on steric effects: Al addition decreases the lattice parameters of the initial BCC alloys. This may result in a reduction of the available volume of the interstitial sites for hydrogen, which could cause a destabilization of the hydride phase. This hypothesis is in line with the proposal by Pineda-Romero in the closely related $Al_x(TiVNb)_{1-x}$ system [18,19].

A comparison to the previous literature data allows to better appreciate the role of Al on the hydride destabilization. The presently observed FCC hydride destabilization (from 278 °C to 190 °C) is not as important as earlier results, where a 10 at.% addition of Al into the TiVNb and $Ti_{0.325}V_{0.275}Zr_{0.125}Nb_{0.275}$ alloys caused a destabilization of FCC hydrides from 241 to 99 °C, and from 270 to 160 °C, respectively [14,18]. This may be tentatively explained by the enthalpies of binary hydride formation (in the CaF_2 prototype), as calculated by Bourgeois and coworkers [53]. The ranking of these values from the less to the more stable binary hydride is the following: V (−38 kJ/mol) > Nb (−47 kJ/mol) > Hf (−118 kJ/mol) > Ti (−122 kJ/mol) > Zr (−146 kJ/mol). In other terms, the presence of Ti, Zr and Hf elements (with values < −100 kJ/mol) in the initial alloys is expected to influence the stability of related hydrides. Consequently, the hydrides might be ranked from the less to the more stable upon the presence of one, two or three of these elements as follows: ***Ti***VNb, $\boldsymbol{Ti}_{0.325}V_{0.275}\boldsymbol{Zr}_{0.125}Nb_{0.275}$ and ***Ti***VNb***ZrHf***. Thus, the expected destabilization effect of Al seems to depend on the chemical composition of alloys, and it appears to have lesser effect on TiVZrNbHf than the already reported two compositions TiVNb and $Ti_{0.325}V_{0.275}Zr_{0.125}Nb_{0.275}$ [14,18].

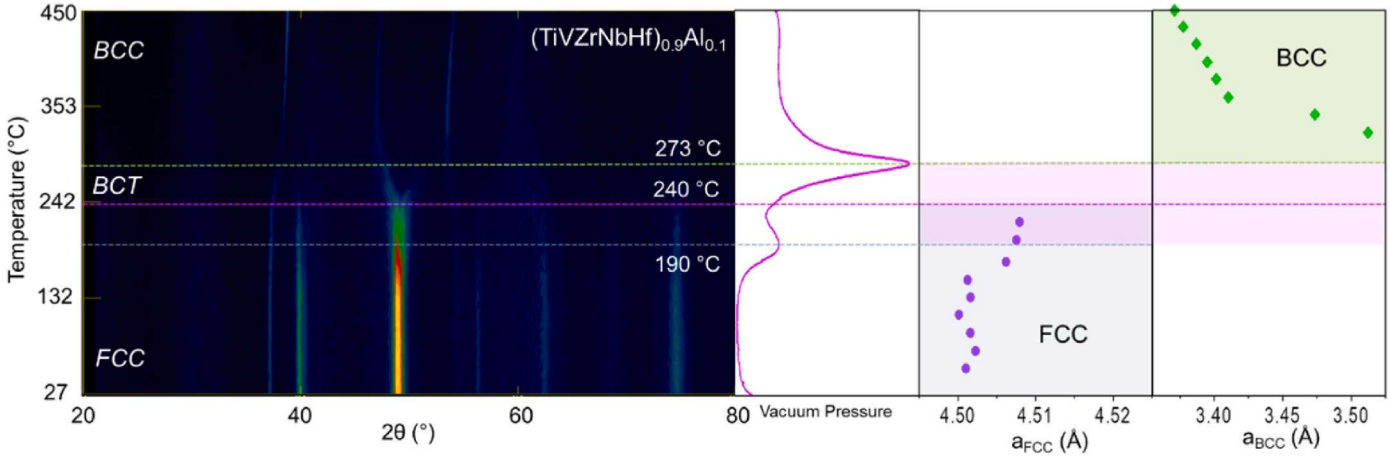


Fig. 5. *In situ* neutron diffraction surface plot (λ = 1.28 Å) for the $(TiVZrNbHf)_{0.90}Al_{0.10}$ composition during deuterium desorption from 27 to 450 °C (1 °C/min) under secondary vacuum. Desorption gas profile (middle panel) and thermal variation of lattice parameters for the FCC deuteride and BCC desorbed phase, as determined from structural analysis.

3.6. Crystalline defects in alloys and hydrides

HEAs are known to possess an important lattice distortion that can be relaxed by defects formation into the crystalline lattice. Moreover, hydrogen absorption and desorption in HEAs may degrade the materials and affect the cycle-life stability of metal hydrides [54]. Various intrinsic degradation reasons have been proposed, which includes decrepitation, sintering, defects formation and H trapping, amorphization and, in some extreme cases, disproportionation [55].

Crystalline defects initially present in this series of HEAs and formed after hydride formation have been characterized by positron annihilation lifetime spectroscopy (PALS) and coincidence Doppler broadening (CDB) spectroscopy. The PALS experiments deliver information about the type and the concentration of the open volume defects, while CDB enables characterization of the local chemical environment of defects [28,56]. The results of PALS for the whole series $(TiVZrNbHf)_{1-x}Al_x$ with $x = 0$, 0.05 and 0.10 as both as-cast alloys and FCC hydrides are listed in Table 3. PALS spectra and fits are given in section 6 of supplementary information.

PALS spectra of all samples studied can be well described by a single component with lifetime τ_1. Some samples demonstrate a weak long-lived component with a lifetime of $\tau_2 = 1.1–1.4$ ns The intensity of this component does not exceed 1 % and it originates from the pick-off annihilation of ortho-positronium (o-Ps) formed in nanoscopic pores. The o-Ps component was detected in the as-cast alloy $(TiVZrNbHf)_{0.90}Al_{0.10}$ and the hydride sample $(TiVZrNbHf)_{0.95}Al_{0.05}$ $H_{1.75}$, suggesting that the alloys may contain a small amount of residual porosity.

Ab-initio calculations of positron lifetimes were conducted to better understand the origin of the component τ_1. The positron lifetimes in the alloys $(TiVZrNbHf)_{1-x}Al_x$ and their hydrides were determined using the methodology outlined in Čížek et al. [57] HEAs were modelled using supercells, where lattice sites were filled randomly with Ti, Zr, Nb, Hf, V, and Al atoms to match the composition of the alloy. For the $(TiVZrNbHf)_{1-x}Al_x$ alloys, a 4 × 4 × 4 (256 atom based) supercell with BCC structure was utilized while a 4 × 4 × 4 (256-atom based) supercell with FCC structure was used for the $(TiVZrNbHf)_{1-x}Al_x$ hydrides. In both cases, the lattice parameters obtained for the respective alloys *via* SR-XRD, and listed in Table 1, were employed in the calculations.

Fig. 6a illustrates the calculated positron density in a perfect (defect-free) $(TiVZrNbHf)_{0.95}Al_{0.05}$ alloy. In this case, the positron is delocalized within the lattice and has the highest probability of being found in interatomic regions. The lifetime of this delocalized positron, known as the bulk positron lifetime, is determined by the overlap of positron and electron densities integrated over the entire supercell. Fig. 6b shows the positron density in a $(TiVZrNbHf)_{0.95}Al_{0.05}$ alloy containing a vacancy. In this scenario, the positron is confined within the vacancy, and its lifetime is influenced by the local electron density that the positron experiences in that space.

In HEAs, the distribution of alloying elements across lattice sites leads to variations in positron lifetimes. To estimate these variations, positron lifetime calculations were performed for 100 supercells constructed using the aforementioned procedure. Histograms of the calculated lifetimes for both free positrons and positrons trapped in vacancies for the $(TiVZrNbHf)_{1-x}Al_x$ alloys and their hydrides are shown in Fig. 7. It is clear from the figure that the spread of positron lifetimes caused by different distributions of alloying elements is greater for positrons trapped in vacancies compared to free positrons that are delocalized in the lattice.

The mean values and standard deviations of positron lifetimes obtained from these calculations are summarized in Table 4. The mean value of positron lifetimes increases with increasing Al content in the alloy, and their range increases as well. The range of bulk positron lifetimes is characterized by standard deviations of 1–2 ps, while for positrons trapped in vacancies, the standard deviation is approximately 5–6 ps. This difference arises because the lifetime of a positron confined in a vacancy is primarily influenced by the chemical nature of its nearest neighbours.

When comparing the experimental positron lifetimes presented in Table 3 with the average values of calculated positron lifetime distributions shown in Tables 4 and it can be concluded that the main component, $\tau_1 = 151$ ps observed in the TiVZrNbHf alloy aligns well with the calculated lifetimes of free positrons that are delocalized in the perfect TiVZrNbHf lattice. This suggests that the defect concentration in the as-cast TiVZrNbHf alloy is very low, leading to positron annihilation primarily in the delocalized state. It is worth noting that a previous report [57] indicated that the closely related composition of TiZrNbHfTa, forms a single-phase random solid solution after annealing at 1000 °C, exhibiting a single-component PALS spectrum and a similar lifetime of 141 ps This further indicates that the as-cast alloy contains a very low concentration of defects and that virtually all positrons are annihilated in the free state.

The addition of Al into TiVZrNbHf results in an increase in the experimental positron lifetime τ_1 (Table 3). The alloy $(TiVZrNbHf)_{0.95}Al_{0.05}$ exhibits $\tau_1 = 159$ ps, which is slightly higher than the mean bulk lifetime of 147 ps calculated for the same alloy. For the $(TiVZrNbHf)_{0.90}Al_{0.10}$ alloy, which has the highest Al content, the lifetime τ_1 increases even further to 180 ps This value is significantly higher than the calculated bulk positron lifetime of 150 ps, suggesting some changes in the positron annihilation sites within alloys containing Al.

Interestingly, while the τ_1 value in these alloys is higher than the calculated bulk positron lifetime, it remains significantly lower than the lifetime expected for positrons trapped in vacancies. The observed lifetime of 180 ps in the $(TiVZrNbHf)_{0.90}Al_{0.10}$ alloy is also close to the calculated bulk lifetimes of 179–184 ps for the hydrides with FCC structure.

SEM-EDS investigations presented in the supplementary information (Section 2) revealed that the $(TiVZrNbHf)_{1-x}Al_x$ alloys with $x = 0.05$ and 0.1, contain small amounts of a secondary phase rich in Al and V. Assuming these alloys contain a secondary phase, it is possible that positrons preferentially annihilate within these grains, which have lower electron density and act as potential wells for positrons. As a result, the lifetime τ_1 is prolonged due to the contribution of positrons that annihilate inside the secondary phase particles. Since the fraction of positrons annihilated in these particles is greater in the alloy with a higher Al content, the prolongation of τ_1 is more pronounced in $(TiVZrNbHf)_{0.90}Al_{0.10}$.

As hydrides, the entire series exhibits a significantly larger main lifetime τ_1 compared to as-cast alloys (Table 3). Also, the observed lifetimes τ_1 for hydrides (Table 3) are higher than the calculated bulk lifetimes for the corresponding hydride phases (Table 4). This suggests

Table 3
Results of the PLAS analysis: lifetimes (τ_i) and relative intensities in brackets of the exponential components resolved in the PALS spectra.

$TiZrNbHfV_{1-x}Al_x$	x	Type	Lattice	Component τ_1 (ps)	Component τ_2 (ns)
TiVZrNbHf	0	As-cast	BCC	151 ± 0.2 (100 %)	–
$(TiVZrNbHf)_{0.95}Al_{0.05}$	0.05			159 ± 0.2 (100 %)	–
$(TiVZrNbHf)_{0.90}Al_{0.10}$	0.10			180 ± 0.2 (99 %)	1.35 ± 0.5 (1 %)
$(TiVZrNbHf)H_{2.0}$	0	Hydride	FCC	193 ± 0.2 (100 %)	
$(TiVZrNbHf)_{0.95}Al_{0.05}$ $H_{1.75}$	0.05			207 ± 0.3 (99 %)	1.13 ± 0.9 (1 %)
$(TiVZrNbHf)_{0.90}Al_{0.10}H_{1.7}$	0.10			213 ± 0.3 (100 %)	

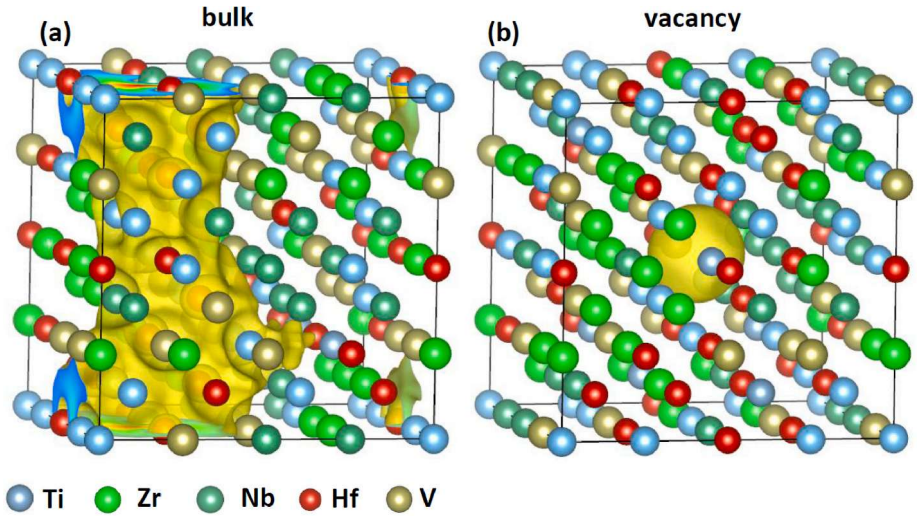


Fig. 6. Isosurface of calculated positron density corresponding to 10 % of maxima for $(TiVZrNbHf)_{0.95}Al_{0.05}$ (a) a perfect (defect-free) supercell; (b) a supercell containing a vacancy.

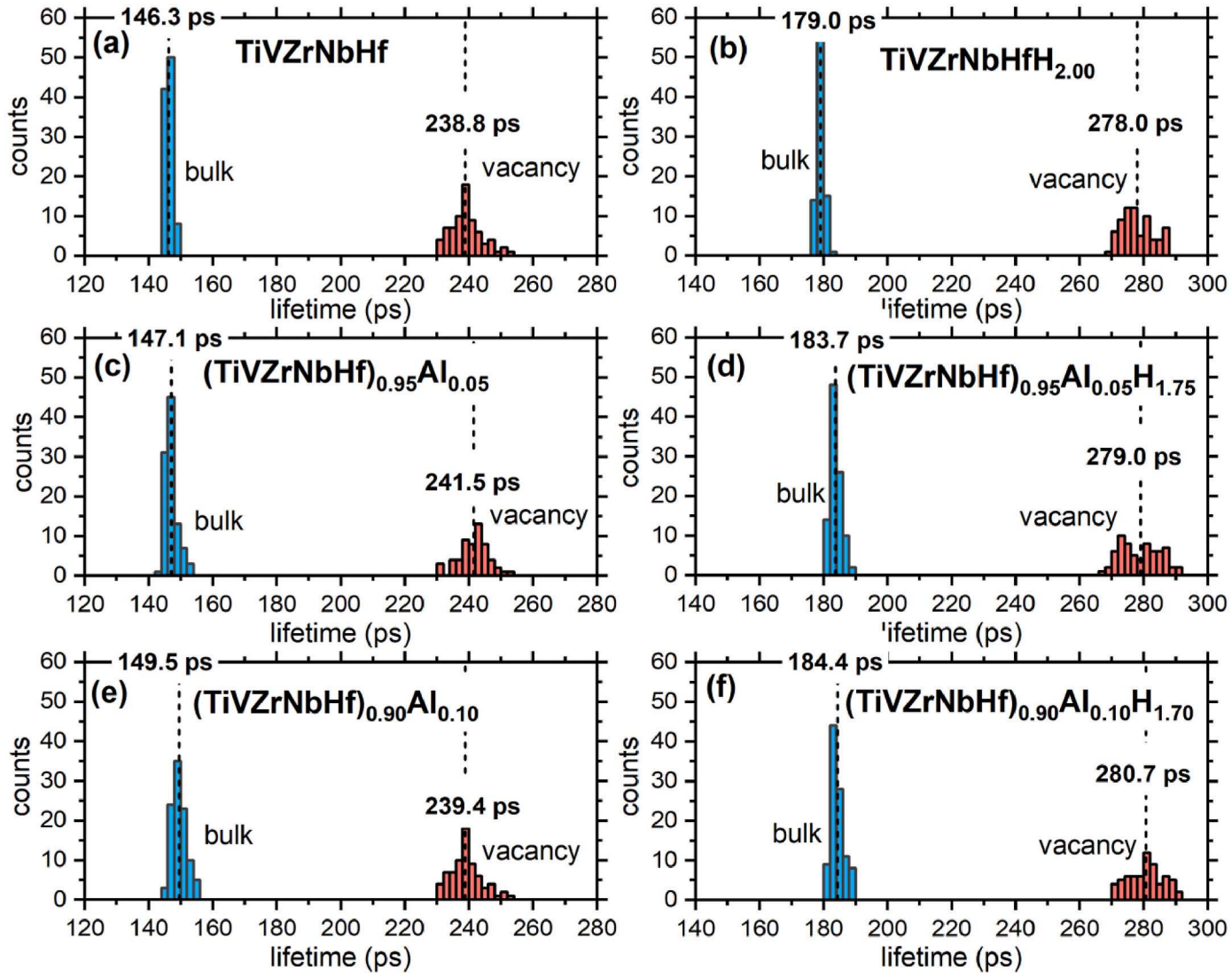


Fig. 7. Histograms of calculated lifetimes of (a) free positrons delocalized in perfect lattice (bulk); (b) positrons trapped in vacancies. Dashed vertical lines and labels indicate average values of positron lifetime distributions.

Table 4
Calculated lifetimes τ_B of free positrons delocalized in defect-free lattice (bulk) and lifetimes τ_V of positrons trapped in vacancies. Positron lifetimes collected in the table represent average values from calculations for 100 supercells with lattice sites randomly filled with alloying elements to match the composition of the alloy. The dispersion of positron lifetimes caused by different distributions of alloying elements is characterized by standard deviations σ_B, σ_V of calculated lifetimes.

$TiZrNbHfV_{1-x}Al_x$	x	bulk		vacancy	
		τ_B (ps)	σ_B (ps)	τ_V (ps)	σ_V (ps)
TiVZrNbHf	0	146.3	1.2	238.8	4.8
$(TiVZrNbHf)_{0.95}Al_{0.05}$	0.05	147.1	1.9	241.5	4.5
$(TiVZrNbHf)_{0.90}Al_{0.10}$	0.10	150	2	225	30
$(TiVZrNbHf)H_{2.0}$	0	179.0	1.0	278.0	4.9
$(TiVZrNbHf)_{0.95}Al_{0.05}$ $H_{1.75}$	0.05	183.7	1.7	279.0	6.0
$(TiVZrNbHf)_{0.90}Al_{0.10}H_{1.7}$	0.10	184.4	2.0	280.7	5.3

that the formation of hydrides leads to the development of open volume lattice defects. At the same time, the lifetimes τ_1 observed for hydrides are shorter than the calculated lifetimes for positrons trapped at vacancies. This indicates that the phase transition to the hydride phase results in the creation of dislocations due to plastic deformation occurring during the growth of hydride, which have a larger specific volume than the matrix of the alloy. Dislocations are characterized by a positron lifetime that is slightly shorter than that of a monovacancy [28], as the dislocation line itself acts as a shallow positron trap [58]. The positron, which is weakly localized in the dislocation, is ultimately trapped and annihilated at a vacancy bound to the dislocation [58]. For a vacancy, it is energetically favourable to reside in the compressive elastic stress field of the dislocation. Consequently, the open volume of the vacancy is 'squeezed' by the compressive strain caused by the dislocation. This is reflected in a positron lifetime that is typically 10–20 ps shorter compared to that of a bare monovacancy [28].

Furthermore, it is known that the presence of hydrogen absorbed in the crystalline lattice lowers the energy required for vacancy formation and facilitates the creation of vacancies [59,60]. Hydrogen-induced vacancies are not bare vacancies; rather, they are complexes of vacancies associated with multiple hydrogen atoms that are bound to the vacancy and situated in interstitial regions between the vacancy and the nearest neighbour ions [61]. The presence of hydrogen atoms bound to vacancies leads to a shortening of the lifetime for trapped positrons [62].

Therefore, it is likely that hydrogenation of $(TiVZrNbHf)_{1-x}Al_x$ alloys introduces both dislocations and vacancies. The concentration of these hydrogen-induced defects (dislocations and vacancies) in the hydrogenated alloys is so high that virtually all positrons are trapped at defects and annihilated in the trapped state. Moreover, the τ_1 observed for hydrides increases with Al content, indicating that the additional element plays a role in the formation of defects with a larger open volume. This might be related to the faster hydrogen absorption kinetics observed in Al-containing alloys (see Fig. 1).

The results of the CDB investigations are presented in Fig. 8 as ratio curves related to a well-annealed pure Al reference (more details on data treatment are given in section 7 of supplementary information). The ratio curves for as-cast $(TiVZrNbHf)_{1-x}Al_x$ alloys exhibit a similar shape, characterized by a peak at $p \approx 10 \times 10^{-3}$ m_0c followed by a broader peak located at $p \approx 30 \times 10^{-3}$ m_0c. As the amount of Al increases, the ratio curves for the $(TiVZrNbHf)_{1-x}Al_x$ alloys gradually shift towards unity, indicating that the peaks become less pronounced. This shift reflects an increasing contribution from positrons that are annihilated near Al atoms. The momentum distribution for positrons annihilated by Al core electrons appears as a straight line at unity since all curves are related to Al.

In the case of hydrides, the ratio curves are suppressed in the high momentum region ($p > 10 \times 10^{-3}$ m_0c). This suppression indicates that hydrides contain open volume defects. Positrons in hydrides are confined within these open volume defects, which reduces the overlap between the positron wave function and the wave functions of the core electrons of the alloy constituents. Therefore, CDB investigations support the understanding that the phase transition of $(TiVZrNbHf)_{1-x}Al_x$ alloys into the hydride phase introduces a high density of open volume defects.

4. Conclusions

The alloys $(TiVZrNbHf)_{1-x}Al_x$ where $x = 0$, 0.05, and 0.10 were synthesised by arc-melting to produce BCC structures, with a minor V-Al-rich phase in Al-containing alloys. With increasing the addition of Al, the lattice parameters of the resulting alloys decreased, closely correlating with a smaller atomic radius of Al compared to the most of elements present. The alloys absorb hydrogen at 25 °C with a decrease in the capacity with increasing Al content ranging from 2.0 to 1.70 H/M. After absorption, they each formed FCC hydride phases, where deuterium atoms occupy tetrahedral interstitial sites, as confirmed through neutron diffraction. PDF analysis confirmed that these materials are random solid solutions, irrespective of BCC and FCC lattices.

XANES investigations revealed the electronic structure of the initial alloys as well changes introduced by FCC hydride formation and corroborated by DFT calculation. The H *s* orbitals hybridize with *s-p* and *d* states of metals forming a low-laying energy band below the Fermi level.

In situ neutron diffraction during deuterium desorption from FCC $(TiVZrNbHf)_{0.90}Al_{0.10}$ deuteride shows a two-step transition from FCC → BCT → recovered BCC lattice. Moreover, the addition of 10 at.% Al destabilizes the FCC hydride phase as compared to the pristine

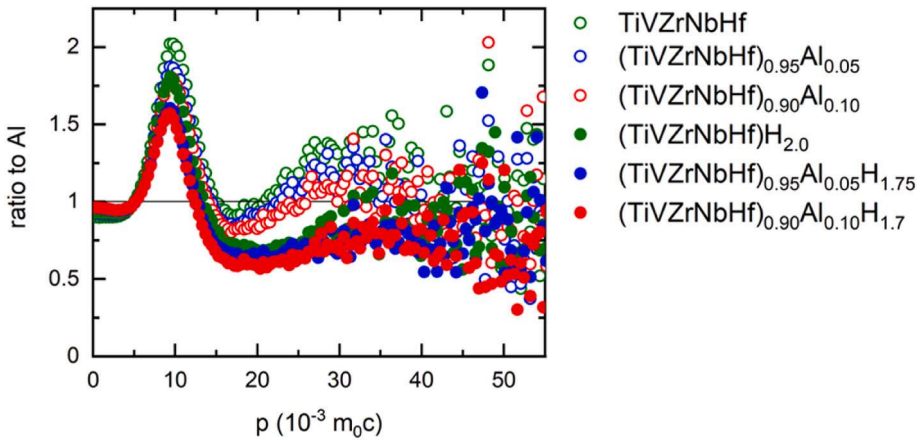


Fig. 8. CDB ratio curves (related to well annealed pure Al) for $(TiVZrNbHf)_{1-x}Al_x$ alloys and their hydrides.

TiVZrNbHf alloy studied previously. In can be concluded that while this agrees with previous results on similar systems published the presence of Hf, an element forming very stable hydride, reduces the influence Al has on destabilising the FCC hydride phase.

Finally, the presence of crystalline defects in these alloys was studied by PALS and CDB before and after hydrogenation. A very low concentration of defects is suggested from the short position lifetime observed into the initial TiVZrNbHf alloy. However, the increased position lifetime measured in the Al-containing alloys suggests the presence of regions of lower electron density that act as potential wells for positrons. *Ab-initio* calculation confirmed by XRD and SEM-EDS investigations seem to indicate that these regions could be the secondary Al-V rich phases that are inevitably formed into Al-containing alloys, as also supported by the CDB experimental data. Furthermore, PALS studies on FCC hydrides suggest the formation of both dislocations and vacancies defects while Al seems to play a role in the formation of larger open volume defects which might play a role in the faster hydrogen absorption kinetics observed in Al-containing alloys.

In conclusion, this work provides an in-depth study on the effect of Al on the phase transformations in high-entropy alloys containing refractory elements that can form high-capacity hydrides indicating the Al induces faster absorption kinetics and a destabilization of the hydride phase.

CRediT authorship contribution statement

Faye Greaves: Writing – review & editing, Writing – original draft, Visualization, Validation, Investigation. **Vivian Nassif:** Writing – review & editing, Resources, Investigation. **Maria Alfredsson:** Writing – review & editing, Resources, Investigation. **Alan V. Chadwick:** Writing – review & editing, Resources, Investigation. **Ryan Parmenter:** Writing – review & editing, Investigation. **Jakub Čížek:** Writing – review & editing, Visualization, Validation, Resources, Investigation. **Oksana Melikhova:** Writing – review & editing, Visualization, Validation. **Lei Lei:** Writing – review & editing, Visualization, Validation, Investigation. **David M. Grant:** Writing – review & editing, Resources, Investigation. **Martin Dornheim:** Writing – review & editing, Resources, Investigation. **Sanliang Ling:** Writing – review & editing, Visualization, Validation, Resources, Investigation. **Patrick Cullen:** Writing – review & editing, Supervision, Investigation. **Claudia Zlotea:** Writing – review & editing, Writing – original draft, Visualization, Validation, Supervision, Resources, Investigation, Conceptualization.

Data statement

The data supporting this article have been included as part of the Supplementary Information.

Funding sources

FG, CZ and PC acknowledge the funding from the Agence de l'Innovation de défense (AID) (Convention N° 2022 65 0054). JC and OM acknowledge support from the Czech Science Foundation (project 25-18077S). Computational resources for *ab-initio* calculations of positron lifetimes were supplied by the project "e-Infrastruktura CZ" (e-INFRA LM2018140) provided within the program Projects of Large Research, Development and Innovations Infrastructures.

Work at the University of Nottingham is supported by EPSRC (EP/V042556/1) and Leverhulme Trust (Grant No. LIP-2021-018). The authors acknowledge the use of the ARCHER2 supercomputer through membership of the UK's HPC Materials Chemistry Consortium, which is funded by EPSRC (EP/X035859/1).

Declaration of competing interest

The authors declare that they have no known competing financial interests or personal relationships that could have appeared to influence the work reported in this paper.

Acknowledgements

Fabrice Couturas, Valérie Lalanne, Olivier Rouleau and Rémy Pires Brazuna from ICMPE (Institut de Chimie et des Matériaux Paris-Est, UMR 7182 CNRS-UPEC, Thiais, France) are acknowledged for their help with hydrogenation, arc-melting, XRD, and SEM-EDX experiments, respectively. FG and CZ thank Sofien Djellit from D1B-ILL (Institut Laue-Langevin, Grenoble, France) for help with neutron diffraction experiments at ILL. We acknowledge Diamond Light Source for access to B18 under the Energy Materials Block Allocation Group (BAG).

Appendix A. Supplementary data

Supplementary data to this article can be found online at https://doi.org/10.1016/j.intermet.2025.109119.

Data availability

Data will be made available on request.

References

[1] P. Nikolaidis, A. Poullikkas, A comparative overview of hydrogen production processes, Renew. Sustain. Energy Rev. 67 (2017) 597–611, https://doi.org/10.1016/j.rser.2016.09.044.
[2] A.M. Elberry, J. Thakur, J. Veysey, Seasonal hydrogen storage for sustainable renewable energy integration in the electricity sector: a case study of Finland, J. Energy Storage 44 (2021) 103474, https://doi.org/10.1016/j.est.2021.103474.
[3] I.A. Hassan, H.S. Ramadan, M.A. Saleh, D. Hissel, Hydrogen storage technologies for stationary and mobile applications: review, analysis and perspectives, Renew. Sustain. Energy Rev. 149 (2021) 111311, https://doi.org/10.1016/j.rser.2021.111311.
[4] J.O. Abe, A.P.I. Popoola, E. Ajenifuja, O.M. Popoola, Hydrogen energy, economy and storage: review and recommendation, Int. J. Hydrogen Energy 44 (2019) 15072–15086, https://doi.org/10.1016/j.ijhydene.2019.04.068.
[5] S. Niaz, T. Manzoor, A.H. Pandith, Hydrogen storage: materials, methods and perspectives, Renew. Sustain. Energy Rev. 50 (2015) 457–469, https://doi.org/10.1016/j.rser.2015.05.011.
[6] B. Cantor, I.T.H. Chang, P. Knight, A.J.B. Vincent, Microstructural development in equiatomic multicomponent alloys, Mater. Sci. Eng., A 375–377 (2004) 213–218, https://doi.org/10.1016/j.msea.2003.10.257.
[7] J. Yeh, S. Chen, S. Lin, J. Gan, T. Chin, T. Shun, C. Tsau, S. Chang, Nanostructured high-entropy alloys with multiple principal elements: novel alloy design concepts and outcomes, Adv. Eng. Mater. 6 (2004) 299–303, https://doi.org/10.1002/adem.200300567.
[8] S. Guo, C.T. Liu, Phase stability in high entropy alloys: formation of solid-solution phase or amorphous phase, Prog. Nat. Sci. Mater. Int. 21 (2011) 433–446, https://doi.org/10.1016/S1002-0071(12)60080-X.
[9] D.B. Miracle, O.N. Senkov, A critical review of high entropy alloys and related concepts, Acta Mater. 122 (2017) 448–511, https://doi.org/10.1016/j.actamat.2016.08.081.
[10] J.-P. Couzinié, G. Dirras, Body-centered cubic high-entropy alloys: from processing to underlying deformation mechanisms, Mater. Char. 147 (2019) 533–544, https://doi.org/10.1016/j.matchar.2018.07.015.
[11] M. Asadikiya, A review of the design of high-entropy aluminum alloys: a pathway for novel Al alloys, J. Mater. Sci. 56 (2021) 12093–12110. https://doi.org/10.1007/s10853-021-06042-6.
[12] K.R. Cardoso, V. Roche, A.M. Jorge Jr., F.J. Antiqueira, G. Zepon, Y. Champion, Hydrogen storage in MgAlTiFeNi high entropy alloy, J. Alloys Compd. 858 (2021) 158357, https://doi.org/10.1016/j.jallcom.2020.158357.
[13] R.B. Strozi, D.R. Leiva, J. Huot, W.J. Botta, G. Zepon, Synthesis and hydrogen storage behavior of Mg–V–Al–Cr–Ni high entropy alloys, Int. J. Hydrogen Energy 46 (2021) 2351–2361, https://doi.org/10.1016/j.ijhydene.2020.10.106.
[14] J. Montero, G. Ek, L. Laversenne, V. Nassif, M. Sahlberg, C. Zlotea, How 10 at% Al addition in the Ti-V-Zr-Nb high-entropy alloy changes hydrogen sorption properties, Molecules 26 (2021) 2470, https://doi.org/10.3390/molecules26092470.
[15] M.M. Nygård, G. Ek, D. Karlsson, M.H. Sørby, M. Sahlberg, B.C. Hauback, Counting electrons - a new approach to tailor the hydrogen sorption properties of high-entropy alloys, Acta Mater. 175 (2019) 121–129, https://doi.org/10.1016/j.actamat.2019.06.002.
[16] G. Ek, M.M. Nygård, A.F. Pavan, J. Montero, P.F. Henry, M.H. Sørby, M. Witman, V. Stavila, C. Zlotea, B.C. Hauback, M. Sahlberg, Elucidating the effects of the composition on hydrogen sorption in TiVZrNbHf-Based high-entropy alloys, Inorg. Chem. 60 (2021) 1124–1132, https://doi.org/10.1021/acs.inorgchem.0c03270.

[17] J. Montero, C. Zlotea, G. Ek, J.-C. Crivello, L. Laversenne, M. Sahlberg, TiVZrNb multi-principal-element alloy: synthesis optimization, structural, and hydrogen sorption properties, Molecules 24 (2019) 2799, https://doi.org/10.3390/molecules24152799.

[18] N. Pineda-Romero, M. Witman, V. Stavila, C. Zlotea, The effect of 10 at.% Al addition on the hydrogen storage properties of the Ti0.33V0.33Nb0.33 multi-principal element alloy, Intermetallics 146 (2022) 107590, https://doi.org/10.1016/j.intermet.2022.107590.

[19] N. Pineda-Romero, C. Zlotea, Uncovering the effect of Al addition on the hydrogen storage properties of the ternary TiVNb alloy, Materials 15 (2022) 7974, https://doi.org/10.3390/ma15227974.

[20] D. Karlsson, G. Ek, J. Cedervall, C. Zlotea, K.T. Møller, T.C. Hansen, J. Bednarčík, M. Paskevicius, M.H. Sørby, T.R. Jensen, U. Jansson, M. Sahlberg, Structure and hydrogenation properties of a HfNbTiVZr high-entropy alloy, Inorg. Chem. 57 (2018) 2103–2110, https://doi.org/10.1021/acs.inorgchem.7b03004.

[21] M. Sahlberg, D. Karlsson, C. Zlotea, U. Jansson, Superior hydrogen storage in high entropy alloys, Sci. Rep. 6 (2016) 36770, https://doi.org/10.1038/srep36770.

[22] F. Greaves, A. Bouzidi, L. Perrière, G. Vaughan, V. Nassif, L. Laversenne, A. Borgschulte, M.L. Martins, Y. Cheng, A.J. Ramirez-Cuesta, P.Á. Szilágyi, P. Cullen, C. Zlotea, Hydrogen induced phase transition in TiZrNbHfV1–xTax high entropy alloys, J. Phys. Chem. C 129 (2025) 2904–2912, https://doi.org/10.1021/acs.jpcc.4c08233.

[23] A. Le Bail, H. Duroy, J.L. Fourquet, Ab-initio structure determination of LiSbWO6 by X-ray powder diffraction, Mater. Res. Bull. 23 (1988) 447–452, https://doi.org/10.1016/0025-5408(88)90019-0.

[24] G.B.M. Vaughan, R. Baker, R. Barret, J. Bonnefoy, T. Buslaps, S. Checchia, D. Duran, F. Fihman, P. Got, J. Kieffer, S.A.J. Kimber, K. Martel, C. Morawe, D. Mottin, E. Papillon, S. Petitdemange, A. Vamvakeros, J.-P. Vieux, M. Di Michiel, ID15A at the ESRF – a beamline for high speed ıt operando X-ray diffraction, diffraction tomography and total scattering, J. Synchrotron Radiat. 27 (2020) 515–528, https://doi.org/10.1107/S1600577519016813.

[25] G. Ashiotis, A. Deschildre, Z. Nawaz, J.P. Wright, D. Karkoulis, F.E. Picca, J. Kieffer, The fast azimuthal integration Python library: pyFAI, J. Appl. Crystallogr. 48 (2015) 510–519, https://doi.org/10.1107/S1600576715004306.

[26] P. Juhás, T. Davis, C.L. Farrow, S.J.L. Billinge, PDFgetX3: a rapid and highly automatable program for processing powder diffraction data into total scattering pair distribution functions, J. Appl. Crystallogr. 46 (2013) 560–566, https://doi.org/10.1107/S0021889813005190.

[27] C.L. Farrow, P. Juhas, J.W. Liu, D. Bryndin, E.S. Božin, J. Bloch, T. Proffen, S.J. L. Billinge, PDFfit2 and PDFgui: computer programs for studying nanostructure in crystals, J. Phys. Condens. Matter 19 (2007) 335219, https://doi.org/10.1088/0953-8984/19/33/335219.

[28] J. Čížek, Characterization of lattice defects in metallic materials by positron annihilation spectroscopy: a review, J. Mater. Sci. Technol. 34 (2018) 577–598, https://doi.org/10.1016/j.jmst.2017.11.050.

[29] F. Bečvář, J. Čížek, I. Procházka, J. Janotová, The asset of ultra-fast digitizers for positron-lifetime spectroscopy, Nucl. Instrum. Methods Phys. Res. Sect. A Accel. Spectrom. Detect. Assoc. Equip. 539 (2005) 372–385, https://doi.org/10.1016/j.nima.2004.09.031.

[30] J. Čížek, PLRF code for decomposition of Positron Lifetime Spectra, Acta Phys. Pol., A 137 (2020) 177–187, https://doi.org/10.12693/APhysPolA.137.177.

[31] J. Čížek, O. Melikhova, T. Vlasák, P. Hruška, D. Starý, F. Lukáč, Characterization of lattice distortions in refractory metal complex concentrated alloys using positron annihilation spectroscopy, Materialia 23 (2022) 101450, https://doi.org/10.1016/j.mtla.2022.101450.

[32] K.G. Lynn, J.R. MacDonald, R.A. Boie, L.C. Feldman, J.D. Gabbe, M.F. Robbins, E. Bonderup, J. Golovchenko, Positron-Annihilation momentum profiles in aluminum: core contribution and the independent-particle model, Phys. Rev. Lett. 38 (1977) 241–244, https://doi.org/10.1103/PhysRevLett.38.241.

[33] J. Čížek, M. Vlček, I. Procházka, Digital spectrometer for coincidence measurement of Doppler broadening of positron annihilation radiation, Nucl. Instrum. Methods Phys. Res. Sect. A Accel. Spectrom. Detect. Assoc. Equip. 623 (2010) 982–994, https://doi.org/10.1016/j.nima.2010.07.046.

[34] A. Michalowicz, J. Moscovici, D. Muller-Bouvet, K. Provost, MAX: multiplatform applications for XAFS, J. Phys. Conf. 190 (2009) 012034.

[35] A. Michalowicz, J. Moscovici, D. Muller-Bouvet, K. Provost, MAX (Multiplatform Applications for XAFS) New features, J. Phys. Conf. 430 (2013) 012016.

[36] G. Kresse, J. Furthmüller, Efficient iterative schemes for ab initio total-energy calculations using a plane-wave basis set, Phys. Rev. B 54 (1996) 11169–11186, https://doi.org/10.1103/PhysRevB.54.11169.

[37] J.P. Perdew, K. Burke, M. Ernzerhof, Generalized gradient approximation made simple, Phys. Rev. Lett. 77 (1996) 3865–3868, https://doi.org/10.1103/PhysRevLett.77.3865.

[38] P.E. Blöchl, Projector augmented-wave method, Phys. Rev. B 50 (1994) 17953–17979, https://doi.org/10.1103/PhysRevB.50.17953.

[39] D. Hobbs, G. Kresse, J. Hafner, Fully unconstrained noncollinear magnetism within the projector augmented-wave method, Phys. Rev. B 62 (2000) 11556–11570, https://doi.org/10.1103/PhysRevB.62.11556.

[40] M. Methfessel, A.T. Paxton, High-precision sampling for Brillouin-zone integration in metals, Phys. Rev. B 40 (1989) 3616–3621, https://doi.org/10.1103/PhysRevB.40.3616.

[41] J. Hu, X. Li, L. Vitos, S. Schönecker, Effects of Mg and Al doping on the desorption energetics and electronic structure of a Ti-V-Zr-Nb alloy hydride, Acta Mater. 277 (2024) 120198, https://doi.org/10.1016/j.actamat.2024.120198.

[42] A. Agafonov, N. Pineda-Romero, M.D. Witman, V. Enblom, M. Sahlberg, V. Nassif, L. Lei, D.M. Grant, M. Dornheim, S. Ling, V. Stavila, C. Zlotea, Promising alloys for hydrogen storage in the compositional space of (TiVNb)100–x(Cr,Mo)x high-entropy alloys, ACS Appl. Mater. Interfaces 17 (2025) 41991–42003, https://doi.org/10.1021/acsami.5c08574.

[43] A. Agafonov, N. Pineda-Romero, M. Witman, V. Nassif, G.B.M. Vaughan, L. Lei, S. Ling, D.M. Grant, M. Dornheim, M. Allendorf, V. Stavila, C. Zlotea, Destabilizing high-capacity high entropy hydrides via earth abundant substitutions: from predictions to experimental validation, Acta Mater. 276 (2024) 120086, https://doi.org/10.1016/j.actamat.2024.120086.

[44] Gordon Aylward, Tristan Findlay, SI chemical data, in: third ed.J. Chem. Educ., vol. 72, 1995 A109, https://doi.org/10.1021/ed072pA109.1.

[45] D.B. Miracle, O.N. Senkov, A critical review of high entropy alloys and related concepts, Acta Mater. 122 (2017) 448–511, https://doi.org/10.1016/j.actamat.2016.08.081.

[46] N. Pineda Romero, M. Witman, K. Harvey, V. Stavila, V. Nassif, E. Elkaïm, C. Zlotea, Large destabilization of (TiVNb)-Based hydrides via (Al, Mo) addition: insights from experiments and data-driven models, ACS Appl. Energy Mater. 6 (2023) 12560–12572, https://doi.org/10.1021/acsaem.3c02696.

[47] M.M. Nygård, W.A. Sławiński, G. Ek, M.H. Sørby, M. Sahlberg, D.A. Keen, B. C. Hauback, Local order in high-entropy alloys and associated deuterides – a total scattering and Reverse Monte Carlo study, Acta Mater. 199 (2020) 504–513, https://doi.org/10.1016/j.actamat.2020.08.045.

[48] A. Fantin, G.O. Lepore, A.M. Manzoni, S. Kasatikov, T. Scherb, T. Huthwelker, F. d'Acapito, G. Schumacher, Short-range chemical order and local lattice distortion in a compositionally complex alloy, Acta Mater. 193 (2020) 329–337, https://doi.org/10.1016/j.actamat.2020.04.034.

[49] T. Yamamoto, Assignment of pre-edge peaks in K-edge x-ray absorption spectra of 3d transition metal compounds: electric dipole or quadrupole? X Ray Spectrom. 37 (2008) 572–584, https://doi.org/10.1002/xrs.1103.

[50] B. Lengeler, R. Zeller, X-ray absorption near-edge structure of metal hydrides, Journal of the Less Common Metals 103 (1984) 337–347, https://doi.org/10.1016/0022-5088(84)90257-1.

[51] S. Mukerjee, J. McBreen, J.J. Reilly, J.R. Johnson, G. Adzic, K. Petrov, M.P. S. Kumar, W. Zhang, S. Srinivasan, In situ X-Ray Absorption spectroscopy studies of metal hydride electrodes, J. Electrochem. Soc. 142 (1995) 2278–2286, https://doi.org/10.1149/1.2044287.

[52] J. Hu, X. Li, L. Vitos, S. Schönecker, Effects of Mg and Al doping on the desorption energetics and electronic structure of a Ti-V-Zr-Nb alloy hydride, Acta Mater. 277 (2024) 120198, https://doi.org/10.1016/j.actamat.2024.120198.

[53] N. Bourgeois, J.-C. Crivello, P. Cenedese, J.-M. Joubert, Systematic first-principles Study of binary metal hydrides, ACS Comb. Sci. 19 (2017) 513–523, https://doi.org/10.1021/acscombsci.7b00050.

[54] R.B. Strozi, M. Witman, V. Stavila, J. Cizek, K. Sakaki, H. Kim, O. Melikhova, L. Perrière, A. Machida, Y. Nakahira, G. Zepon, W.J. Botta, C. Zlotea, Elucidating primary degradation mechanisms in High-Cycling-Capacity, compositionally tunable high-entropy hydrides, ACS Appl. Mater. Interfaces 15 (2023) 38412–38422, https://doi.org/10.1021/acsami.3c05206.

[55] F.T. Zohra, C.J. Webb, K.E. Lamb, E.MacA. Gray, Degradation of metal hydrides in hydrogen-based thermodynamic machines: a review, Int. J. Hydrogen Energy 64 (2024) 417–438, https://doi.org/10.1016/j.ijhydene.2024.03.228.

[56] F. Tuomisto, Identification of point defects in multielement compounds and alloys with Positron annihilation spectroscopy: challenges and opportunities, Physica Rapid Research Ltrs 15 (2021) 2100177, https://doi.org/10.1002/pssr.202100177.

[57] J. Čížek, T. Vlasák, O. Melikhova, Characterization of lattice defects in refractory metal high-entropy alloy HfNbTaTiZr by means of Positron annihilation spectroscopy, Phys. Status Solidi 219 (2022) 2100840, https://doi.org/10.1002/pssa.202100840.

[58] L.C. Smedskjaer, M. Manninen, M.J. Fluss, An alternative interpretation of positron annihilation in dislocations, J. Phys. F Met. Phys. (1980) 2237.

[59] Y. Fukai, N. Okuma, Formation of superabundant vacancies in Pd hydride under high hydrogen pressures, Phys. Rev. Lett. (1994) 1640–1643.

[60] A. Pundt, R. Kirchheim, Hydrogen IN metals: microstructural aspects, Annu. Rev. Mater. Res. 36 (2006) 555–608, https://doi.org/10.1146/annurev.matsci.36.090804.094451.

[61] W. Xing, X.-Q. Chen, Q. Xie, G. Lu, D. Li, Y. Li, Unified mechanism for hydrogen trapping at metal vacancies, Int. J. Hydrogen Energy 39 (2014) 11321–11327, https://doi.org/10.1016/j.ijhydene.2014.05.032.

[62] J. Cizek, I. Prochazka, S. Danis, M. Cieslar, G. Brauer, W. Anwand, R. Kirchheim, A. Pundt, Hydrogen-induced defects in niobium, J. Alloys Compd. (2007) 446–447, https://doi.org/10.1016/j.jallcom.2006.11.105, 479–483.